Transdermal cold atmospheric plasma-mediated immune checkpoint blockade therapy

Guojun Chen[a,b,c,1], Zhitong Chen[d,1], Di Wen[a,b,c], Zejun Wang[a,b,c], Hongjun Li[a,b,c], Yi Zeng[a,b,c], Gianpietro Dotti[e], Richard E. Wirz[d,2], and Zhen Gu[a,b,c,f,2]

[a]Department of Bioengineering, University of California, Los Angeles, CA 90095; [b]Jonsson Comprehensive Cancer Center, University of California, Los Angeles, CA 90095; [c]California NanoSystems Institute, University of California, Los Angeles, CA 90095; [d]Department of Mechanical and Aerospace Engineering, University of California, Los Angeles, CA 90095; [e]Lineberger Comprehensive Cancer Center, University of North Carolina, Chapel Hill, NC 27514; and [f]Center for Minimally Invasive Therapeutics, University of California, Los Angeles, CA 90095

Edited by David A. Weitz, Harvard University, Cambridge, MA, and approved January 9, 2020 (received for review October 12, 2019)

Despite the promise of immune checkpoint blockade (ICB) therapy against cancer, challenges associated with low objective response rates and severe systemic side effects still remain and limit its clinical applications. Here, we described a cold atmospheric plasma (CAP)-mediated ICB therapy integrated with microneedles (MN) for the transdermal delivery of ICB. We found that a hollow-structured MN (hMN) patch facilitates the transportation of CAP through the skin, causing tumor cell death. The release of tumor-associated antigens then promotes the maturation of dendritic cells in the tumor-draining lymph nodes, subsequently initiating T cell-mediated immune response. Anti-programmed death-ligand 1 antibody (aPDL1), an immune checkpoint inhibitor, released from the MN patch further augments the antitumor immunity. Our findings indicate that the proposed transdermal combined CAP and ICB therapy can inhibit the tumor growth of both primary tumors and distant tumors, prolonging the survival of tumor-bearing mice.

drug delivery | immune checkpoint blockade | cold atmospheric plasma | microneedle | cancer immunotherapy

The immune checkpoint blockade (ICB) increases antitumor immunity by inhibiting intrinsic down-regulators of immunity, and has greatly transformed the landscape of human cancer therapeutics (1–4). However, the overall objective rate of ICB remains modest (4–7), while the occurrence of severe side effects emphasizes the essential need for delivery approaches of ICB therapeutics (8–11). Local delivery of immune checkpoint inhibitors to the targeted sites could be a desirable approach to minimize those limitations and augment the therapeutic efficacy (10, 12).

Plasma, the fourth state of matter (solid, liquid, gas, and plasma) comprising over 99% of the visible universe, is an ionized gas composed of positively/negatively charged species, neutral species, radicals, and photons (13). Cold atmospheric plasma (CAP) devices, which operate at atmospheric pressure and room temperature, have great potential for biomedical applications, including cancer therapy (14, 15). The anticancer effect of CAP mainly relies on the synergistic action of reactive oxygen species (ROS) and reactive nitrogen species (RNS) with the target tissue (14, 15). However, CAP efficacy remains unsatisfactory since the penetration of CAP into tumor tissues is limited, requiring multiple and frequent CAP treatments to achieve desirable therapeutic effects.

Here, we explore the potential of microneedle (MN)-array patch-based transdermal delivery (16–18) that combines CAP and ICB (Fig. 1). We leverage the hollow-structured microneedle (hMN) patch as microchannels to allow CAP to be delivered through the skin into tumors. Cancer cell death induced by CAP releases tumor-associated antigens and promotes dendritic cell (DC) maturation in the tumor-draining lymph node, where DCs can present the major histocompatibility complex-peptide to T cells (19, 20). Subsequent T cell-mediated immune response is initiated and can be further augmented by checkpoint inhibitor, such as anti-programmed death-ligand 1 antibody (aPDL1), included into the hMN patches. We hypothesize that the synergism between CAP and ICB provides a broad platform to promote tumor elimination.

Results

The CAP device (*SI Appendix*, Fig. S1) consisted of a two-electrode assembly connected to the high voltage transformer. The parameters of the CAP device for stable operation and high species delivery efficiency were as follows: peak-peak voltage ∼11 kV and discharge frequency ∼12 kHz (*SI Appendix*, Fig. S2*A*). The feeding gas for this study was industrial purity helium (99.996% purity) with a 16.5 L/min gas flow rate. The optical emission spectrum (OES) indicated the generation of both ROS and RNS (21, 22), while optical and temperature monitoring confirmed the formation of CAP (*SI Appendix*, Fig. S2 *B*–*D*).

After CAP treatment, ROS and RNS were detected in both cells and culture media, and the extents were elevated with increased treatment time (*SI Appendix*, Fig. S3). Cell death induced by CAP was validated in B16F10 melanoma cells. CAP caused immunogenic cell death (ICD), which correlates with the generation of ROS/RNS. Longer CAP treatment led to higher cell death rate and higher expression of calreticulin (CRT, an ICD marker (23)) (*SI Appendix*, Fig. S4 *A* and *B*). Tumor-associated

Significance

Strategies to improve efficacy and reduce side effects of immune checkpoint blockade (ICB) therapy are clinically relevant. Here, we described a transdermal cold atmospheric plasma (CAP)-mediated ICB therapy. Local delivery of CAP through hollow-structured microneedles as microchannels promote the release of tumor-associated antigens by CAP. The subsequent T cell-mediated immune response can be augmented by the immune checkpoint inhibitors delivered via microneedles, resulting in enhanced local and systemic anticancer immunity. The synergism between CAP and ICB integrated with microneedles provides a platform technique for cancer treatment and other diseases in a minimally invasive manner.

Author contributions: G.C., Z.C., R.E.W., and Z.G. designed research; G.C., Z.C., D.W., Z.W., H.L., and Y.Z. performed research; G.C., Z.C., D.W., Z.W., H.L., G.D., R.E.W., and Z.G. analyzed data; and G.C., Z.C., G.D., R.E.W., and Z.G. wrote the paper.

Competing interest statement: G.C., Z.C., R.E.W., and Z.G. have applied for patents related to this study.

This article is a PNAS Direct Submission.

[1]G.C. and Z.C. contributed equally to this work.

[2]To whom correspondence may be addressed. Email: wirz@ucla.edu or guzhen@ucla.edu.

This article contains supporting information online at https://www.pnas.org/lookup/suppl/doi:10.1073/pnas.1917891117/-/DCSupplemental.

First published February 6, 2020.

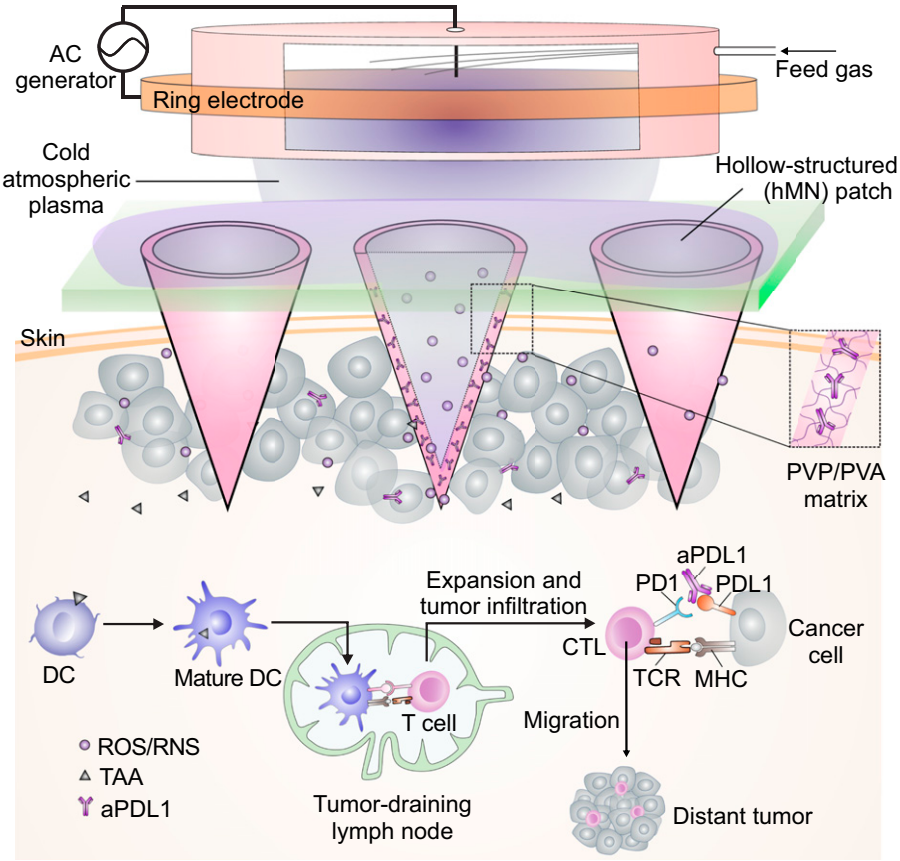

Fig. 1. Illustration of the transdermal cold atmospheric plasma (CAP)-mediated immune checkpoint blockade (ICB) therapy. Schematic of the transdermal combination of CAP and ICB therapy assisted by the polymeric hollow-structured microneedle patch loaded with aPDL1. Nomenclature: DC, dendritic cell; TAA, tumor-associated antigen; CTL, cytotoxic T lymphocyte; TCR, T cell receptor; MHC, major histocompatibility complex; PVP, polyvinylpyrrolidone; PVA, polyvinyl alcohol; ROS, reactive oxygen species; RNS, reactive nitrogen species; AC, alternating current.

antigens released during cell death could be effectively engulfed by immature DCs that process antigens into peptides during their migration to tumor-draining lymph nodes (24–26). Therefore, we studied the immunological effects of CAP on cancer cells toward bone marrow-derived DCs in a transwell assay. It was verified that CAP treatment of B16F10 cells promoted DC maturation in vitro (*SI Appendix*, Fig. S4 *C* and *D*) as indicated by the up-regulation of CD80 and CD86 markers.

The hMN patch was made of the mixture of two biocompatible polymers, polyvinylpyrrolidone (PVP) and polyvinyl alcohol (PVA), where PVP supports the mechanical strength of MNs and PVA slows down the dissociation of MN patches upon fluids. An array of 15 × 15 MNs, with each MN spaced 600 μm center to center, was used for all tests. Each MN is conical with a height of 700 μm and a diameter of 300 μm at the base. SEM images show the formation of an evenly distributed array of equally sized hollow conical MN structures that comprise the hMN patch (Fig. 2*A*). Each MN exhibited a hollow structure closed at the tip and with a ~200 μm diameter opening at the base, indicating a sheath thickness of ~50 μm. The hollow structure and uniformity of shell thickness were confirmed by the 3-dimensional (3D) confocal laser scanning microscopy images (CLSM, rhodamine-loaded MN patch, Fig. 2*B* and Movie S1). Measurement of mechanical strength suggested a failure force for the hollow-structured MNs to be 0.23 N/needle, demonstrating sufficient strength for skin insertion (*SI Appendix*, Fig. S5) (27).

We then investigated whether the hMN patch can serve as microchannels to facilitate CAP penetration. A CAP jet was applied to the hMN patch. Strong CAP observation under the hMN patch (Fig. 2*C*) indicated successful penetration of CAP through the hMN patch. The OES also confirmed that CAP penetrated through an hMN patch exhibited a similar composition compared to the original CAP, with significant amounts of ROS/RNS retained (Fig. 2 *D* and *E*). In contrast, minimal CAP signals were detected when the solid MN (sMN) patch or the mouse skin was applied (*SI Appendix*, Fig. S6). On the other hand, CAP signals penetrated through the mouse skin were greatly enhanced when the hMN patch was applied (*SI Appendix*, Fig. S6*D*), demonstrating a beneficial role of hMN for CAP delivery. Furthermore, CAP did not alter the morphology of MN patches as revealed by SEM images (*SI Appendix*, Fig. S7). hMN patches can also be embedded with aPDL1 during MN patch fabrication. aPDL1 was then released from hMN patch in a sustained manner with 79% being released within 24 h, and aPDL1 maintained its binding affinity toward PDL1 (*SI Appendix*, Fig. S8). Blank hMN patches did not cause detectable cytotoxicity to the cells (*SI Appendix*, Fig. S9). In addition, no significant inflammation was detected in the skin 3 d post MN application as compared to the untreated skin, indicating a good biocompatibility of the hMN patch (*SI Appendix*, Fig. S10).

On the basis of the aforementioned results, we next evaluated the in vivo antitumor activity of this platform. Firstly, we tested whether hMN-assisted CAP induces cancer cell death and triggers DC maturation in B16F10 melanoma-bearing mice. Mice received one-course treatment of CAP, CAP through sMN (sMN/CAP), or CAP through hMN (hMN/CAP) (CAP

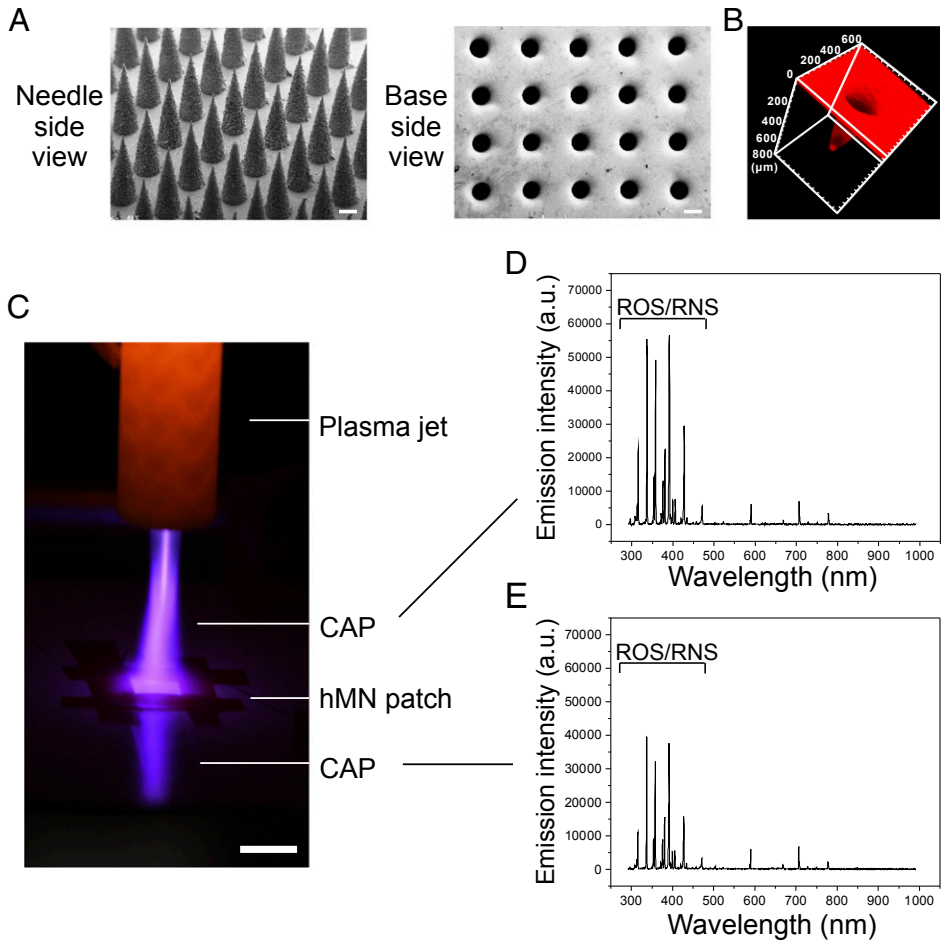

Fig. 2. Characterization of the hollow-structured microneedle (hMN) patch. (*A*) Representative SEM images of the hMN patch from views of needle side and base side. (*B*) A 3D CLSM image of hMN patch (rhodamine loaded). (*C*) Penetration test of the CAP through hMN patch. (Scale bar, 1 cm.) The CAP through the hMN included reactive species and reflection. Representative OES spectra of the CAP (*D*) above hMN patch and (*E*) penetrating through the hMN patch.

treatment: 4 min) (Fig. 3*A*). No temperature changes were detected in the CAP-treated areas, excluding the photothermal cell-killing effect (*SI Appendix*, Fig. S11). The TUNEL assay (*SI Appendix*, Fig. S12) demonstrated that hMN/CAP treatment induced significantly higher cancer cell death as compared to controls, indicating that hMN facilitated the CAP transportation toward tumors and caused cell death in vivo. Consistently, we also observed enhanced DC maturation ($CD86^+CD80^+$ DCs) in the hMN/CAP treatment group, while direct CAP or sMN/CAP did not promote DC maturation (Fig. 3 *B* and *C*).

Mature DCs initiate T cell-mediated immune responses (24). Hence, we monitored tumor growth in mice treated with a single course of CAP, sMN/CAP, hMN/CAP, hMN-aPDL1, and hMN-aPDL1/CAP (aPDL1: 200 μg; CAP treatment: 4 min; Fig. 3*D*). Tumor growth was monitored via bioluminescence signals of B16F10-fLuc cells (Fig. 3*E*). Neither CAP nor sMN/CAP caused tumor regression, suggesting the limited penetration of CAP through the skin or sMN. In contrast, hMN/CAP caused delayed tumor growth compared with the untreated mice (Fig. 3 *F* and *G*). Mice treated with hMN-aPDL1 also exhibited some tumor control as compared with the untreated mice, but mice receiving hMN-aPDL1/CAP exhibited the most significant control of tumor growth that translated into prolonged survival (Fig. 4*H*).

In additional experiments, tumors were harvested 3 d post-treatment for flow cytometric analyses and immunofluorescence staining. Tumor-infiltrating lymphocytes (TILs, $CD3^+$) were increased in the tumors treated with hMN-aPDL1/CAP (Fig. 3*I*). Both $CD8^+$ and $CD4^+$ T cells were increased in mice treated with hMN-aPDL1/CAP (Fig. 3 *J* and *K* and *SI Appendix*, Figs. S13 and S14), while regulatory T cells (Tregs) were decreased (28–30) (*SI Appendix*, Fig. S15). Moreover, $CD8^+$ T cells coexpressing cytotoxic protein granzyme B (GzmB) and cell proliferation marker K_i67 were also increased in the mice receiving hMN-aPDL1/CAP (*SI Appendix*, Figs. S16 and S17). The elevated levels of cytokine secretion, including IFN-γ, IL-6, IL-12p70, IL-2, and TNF-α, further substantiated the effective immune response induced by hMN-aPDL1/CAP treatment (*SI Appendix*, Fig. S18) (31).

With confirmation that hMN-aPDL1/CAP induced locally anticancer immunity, we investigated whether the local effect induced by hMN-aPDL1/CAP can trigger a systemic immune response (32). B16F10 cancer cells were inoculated on both right and left flanks of each mouse. The tumor on the right flank as the primary tumor was treated with hMN-aPDL1/CAP, while the tumor on the opposite site received no treatment (Fig. 4*A*) (33). Tumor bioluminescence signal and tumor size significantly decreased in the mice treated with hMN-aPDL1/CAP as compared with the untreated control (Fig. 4 *B* and *C*). Moreover, the left tumors (distant tumors) in the treated mice were also effectively regressed as compared with those in the untreated mice. Consistently, the weights of primary and distant tumors in the treated mice were also lower than those in the untreated

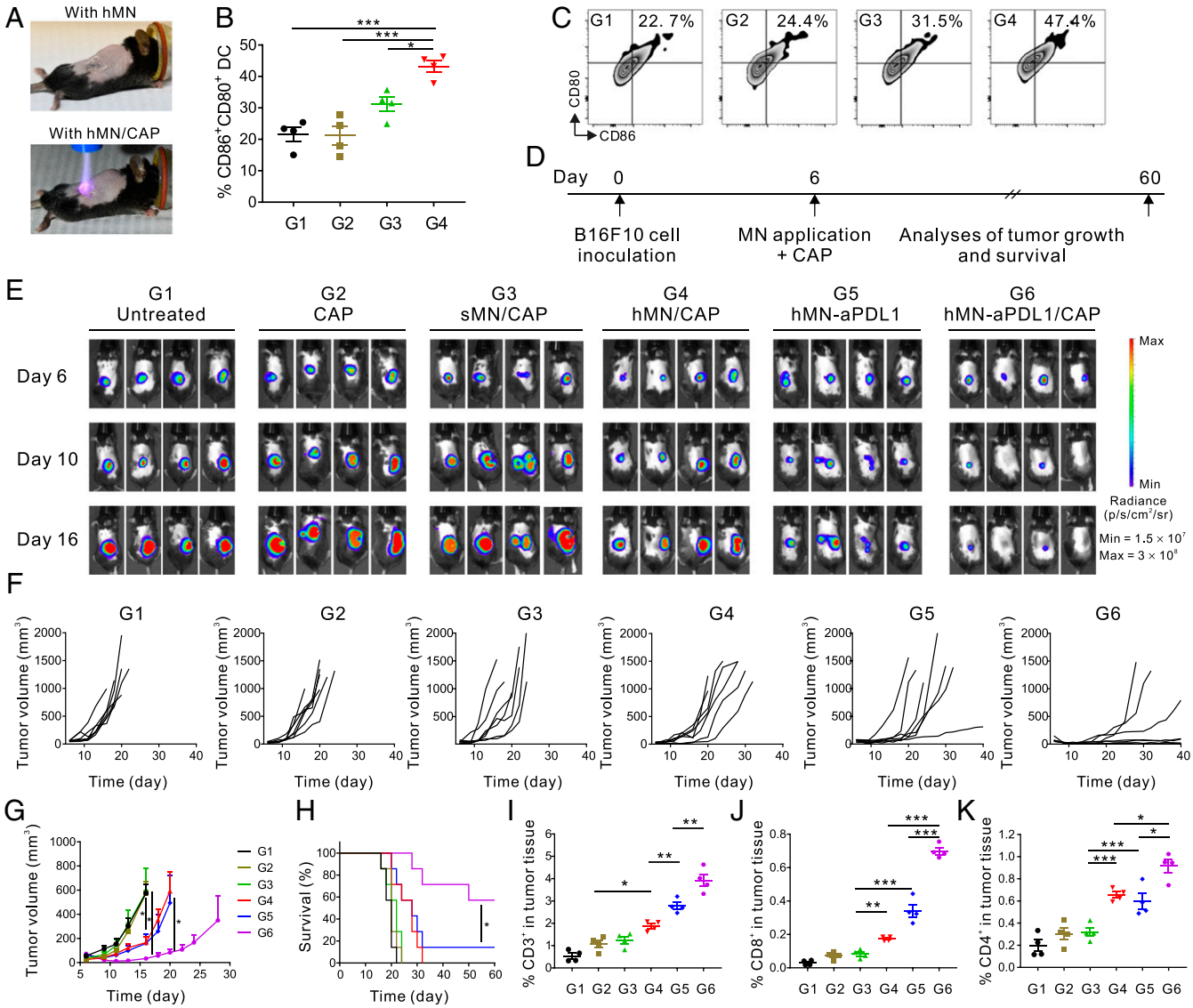

Fig. 3. Combination of CAP and hMN-aPDL1 inhibits B16F10 melanoma growth in vivo. (*A*) Schematic of B16F10 melanoma-bearing mice treated either with the hMN path (*Upper* image) or hMN/CAP (*Lower* image). (*B*) Quantification and (*C*) representative flow cytometry plots of DC maturation in vivo in the tumor-draining lymph nodes. Cells in the tumor-draining lymph nodes were collected 3 d after the treatments (G1: untreated; G2: CAP; G3: sMN/CAP; and G4: hMN/CAP) for assessment by flow cytometry. (*D*) Schematic of the treatment schedule. (*E*) In vivo tumor bioluminescence of the untreated mice and mice treated with CAP, sMN/CAP, hMN/CAP, hMN-aPDL1, and hMN-aPDL1/CAP (aPDL1: 200 μg; CAP treatment: 4 min). Four representative mice per treatment group are shown. (*F*) Individual and (*G*) average tumor growth kinetics in experimental groups ($n = 7$). Growth curves were stopped when the first mouse of the corresponding group died. Data are presented as mean ± SEM. (*H*) Kaplan-Meier survival curves for treated and control mice ($n = 7$). Statistical significance was calculated via the log-rank (Mantel-Cox) test. $^*P < 0.05$; $^{**}P < 0.01$; $^{***}P < 0.001$. Intratumoral (*I*) $CD3^+$ T cells, (*J*) $CD8^+$ T cells, and (*K*) $CD4^+$ T cells in the B16F10 tumor detected 3 d after treatments ($n = 4$). Data are presented as mean ± SEM. Statistical significance was calculated via one-way ANOVA with a Tukey post hoc test for multiple comparisons. $^*P < 0.05$; $^{**}P < 0.01$; $^{***}P < 0.001$.

mice (Fig. 4*D*). The increased numbers of TILs ($CD3^+$), $CD4^+$, and $CD8^+$ T cells (Fig. 4 *E*–*G*) in both treated tumors and distant tumors, and elevated levels of cytokine secretion (*SI Appendix*, Fig. S19) confirmed the activation of a systematic immune response.

Leveraging the unique hollow structure as microchannels, the hMNs can effectively deliver CAP through the skin, interacting with the tumor tissue. The resulting antigen presentation by DCs and T cell-mediated immune response augmented by immune checkpoint inhibitors from the hMN patch further boost anti-cancer immunity locally and systemically. The proposed local treatment strategy can also potentially minimize ICB-related systemic side effects. Of note, integrated with the latest MN-assisted treatments beyond skin-associated diseases (34, 35), this minimally invasive and painless method can be extended to treat different cancer types and a variety of diseases.

Materials and Methods

MN Patch Fabrication. All MN patches were prepared using silicone molds with arrays of conical holes. Polymer solution was directly deposited by pipetting onto the silicone mold surface which was pretreated with deionized water. After desiccation was completed, needle arrays were separated from the silicone molds.

In Vivo Studies. 1×10^6 B16F10-fLuc cells were transplanted into the right flanks of mice. Six days later, tumor-bearing mice were treated one time with either CAP, sMN/CAP, hMN/CAP, hMN-aPDL1, or hMN-aPDL1/CAP. Mice without any

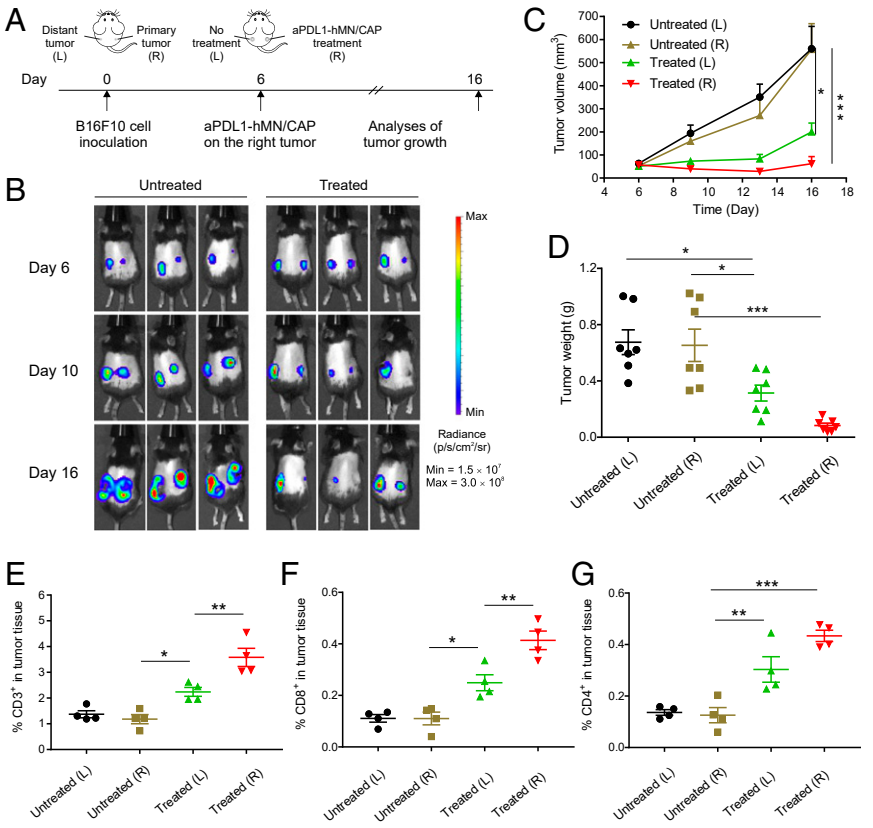

Fig. 4. CAP and hMN-aPDL1 inhibit distant tumor growth. (*A*) Schematic of the treatment schedule. Tumors on the right side were designated as "primary tumor" and were treated with hMN-aPDL1/CAP, and tumors on the left side were designated as "metastatic tumor" and were not treated ($n = 7$). (*B*) In vivo tumor bioluminescence images of the untreated mice and treated mice. Three representative mice per treatment group are shown. (*C*) Left and right tumor growth curves and (*D*) tumor weights of the mice untreated and treated with hMN-aPDL1/CAP. Intratumoral (*E*) $CD3^+$ T cells, (*F*) $CD8^+$ T cells, and (*G*) $CD4^+$ T cells in the B16F10 tumor detected 3 d posttreatment ($n = 4$). Data are presented as mean ± SEM. Statistical significance was calculated via one-way ANOVA with a Tukey post hoc test for multiple comparisons. $^*P < 0.05$; $^{**}P < 0.01$; $^{***}P < 0.001$.

treatment served as control. For the distant tumor model, 1×10^6 B16F10-fLuc cells were inoculated into both left and right flanks of mice. Tumors in the right flank were treated with hMN-aPDL1/CAP as described above.

Detailed experimental procedures for MN preparation and characterization, in vitro aPDL1 release, in vivo animal studies, flow cytometry, immunofluorescence staining, and cytokine detection are provided in *SI Appendix*. The animal study protocol was approved by the Institutional Animal Care and Use Committee at the University of California, Los Angeles.

Data Availability. All data are available within this manuscript and the associated *SI Appendix*.

ACKNOWLEDGMENTS. This work was supported by grants from the start-up packages of University of California, Los Angeles (UCLA), NIH (R01 CA234343-01A1), Air Force Office of Scientific Research (FA9550-14-10317, UCLA Subaward No. 60796566-114411), and Jonsson Comprehensive Cancer Center at UCLA.

1. P. Sharma, J. P. Allison, The future of immune checkpoint therapy. *Science* **348**, 56–61 (2015).
2. D. M. Pardoll, The blockade of immune checkpoints in cancer immunotherapy. *Nat. Rev. Cancer* **12**, 252–264 (2012).
3. W. Zou, J. D. Wolchok, L. Chen, PD-L1 (B7-H1) and PD-1 pathway blockade for cancer therapy: Mechanisms, response biomarkers, and combinations. *Sci. Transl. Med.* **8**, 328rv4 (2016).
4. A. Ribas, J. D. Wolchok, Cancer immunotherapy using checkpoint blockade. *Science* **359**, 1350–1355 (2018).
5. P. Sharma, J. P. Allison, Immune checkpoint targeting in cancer therapy: Toward combination strategies with curative potential. *Cell* **161**, 205–214 (2015).
6. S. L. Topalian, J. M. Taube, R. A. Anders, D. M. Pardoll, Mechanism-driven biomarkers to guide immune checkpoint blockade in cancer therapy. *Nat. Rev. Cancer* **16**, 275–287 (2016).
7. J. Sunshine, J. M. Taube, PD-1/PD-L1 inhibitors. *Curr. Opin. Pharmacol.* **23**, 32–38 (2015).
8. M. A. Postow, R. Sidlow, M. D. Hellmann, Immune-related adverse events associated with immune checkpoint blockade. *N. Engl. J. Med.* **378**, 158–168 (2018).
9. C. Boutros *et al.*, Safety profiles of anti-CTLA-4 and anti-PD-1 antibodies alone and in combination. *Nat. Rev. Clin. Oncol.* **13**, 473–486 (2016).
10. Q. Chen, C. Wang, G. Chen, Q. Hu, Z. Gu, Delivery strategies for immune checkpoint blockade. *Adv. Healthc. Mater.* **7**, e1800424 (2018).
11. J. E. Salem *et al.*, Cardiovascular toxicities associated with immune checkpoint inhibitors: An observational, retrospective, pharmacovigilance study. *Lancet Oncol.* **19**, 1579–1589 (2018).
12. C. Wang, Y. Ye, G. M. Hochu, H. Sadeghifar, Z. Gu, Enhanced cancer immunotherapy by microneedle patch-assisted delivery of anti-PD1 antibody. *Nano Lett.* **16**, 2334–2340 (2016).
13. A. Piel, *Plasma Physics: An Introduction to Laboratory, Space, and Fusion Plasmas* (Springer, 2017).
14. M. Laroussi, T. Akan, Arc-free atmospheric pressure cold plasma jets: A review. *Plasma Process. Polym.* **4**, 777–788 (2007).
15. M. Keidar *et al.*, Cold atmospheric plasma in cancer therapy. *Phys. Plasmas* **20**, 057101 (2013).
16. M. R. Prausnitz, R. Langer, Transdermal drug delivery. *Nat. Biotechnol.* **26**, 1261–1268 (2008).
17. Y. Ye, J. Yu, D. Wen, A. R. Kahkoska, Z. Gu, Polymeric microneedles for transdermal protein delivery. *Adv. Drug Deliv. Rev.* **127**, 106–118 (2018).
18. M. R. Prausnitz, S. Mitragotri, R. Langer, Current status and future potential of transdermal drug delivery. *Nat. Rev. Drug Discov.* **3**, 115–124 (2004).
19. J. Banchereau, A. K. Palucka, Dendritic cells as therapeutic vaccines against cancer. *Nat. Rev. Immunol.* **5**, 296–306 (2005).
20. D. S. Leventhal *et al.*, Dendritic cells coordinate the development and homeostasis of organ-specific regulatory T cells. *Immunity* **44**, 847–859 (2016).
21. G. Neretti *et al.*, Characterization of a plasma source for biomedical applications by electrical, optical, and chemical measurements. *Plasma Process. Polym.* **15**, 1800105 (2018).
22. J. Kapaldo, X. Han, S. Ptasinska, Shielding-gas-controlled atmospheric pressure plasma jets: Optical emission, reactive oxygen species, and the effect on cancer cells. *Plasma Process. Polym.* **16**, 1800169 (2019).
23. Q. Chen *et al.*, Nanoparticle-enhanced radiotherapy to trigger robust cancer immunotherapy. *Adv. Mater.* **31**, e1802228 (2019).

24. S. C. Eisenbarth, Dendritic cell subsets in T cell programming: Location dictates function. *Nat. Rev. Immunol.* **19**, 89–103 (2019).
25. E. J. Pearce, B. Everts, Dendritic cell metabolism. *Nat. Rev. Immunol.* **15**, 18–29 (2015).
26. Q. Chen *et al*., Photothermal therapy with immune-adjuvant nanoparticles together with checkpoint blockade for effective cancer immunotherapy. *Nat. Commun.* **7**, 13193 (2016).
27. S. P. Sullivan *et al*., Dissolving polymer microneedle patches for influenza vaccination. *Nat. Med.* **16**, 915–920 (2010).
28. M. A. Curran, W. Montalvo, H. Yagita, J. P. Allison, PD-1 and CTLA-4 combination blockade expands infiltrating T cells and reduces regulatory T and myeloid cells within B16 melanoma tumors. *Proc. Natl. Acad. Sci. U.S.A.* **107**, 4275–4280 (2010).
29. V. Sasidharan Nair, E. Elkord, Immune checkpoint inhibitors in cancer therapy: A focus on T-regulatory cells. *Immunol. Cell Biol.* **96**, 21–33 (2018).
30. S. Brahmachari, K. Pahan, Myelin basic protein priming reduces the expression of Foxp3 in T cells via nitric oxide. *J. Immunol.* **184**, 1799–1809 (2010).
31. Q. Chen *et al*., In situ sprayed bioresponsive immunotherapeutic gel for post-surgical cancer treatment. *Nat. Nanotechnol.* **14**, 89–97 (2019).
32. W. Ngwa *et al*., Using immunotherapy to boost the abscopal effect. *Nat. Rev. Cancer* **18**, 313–322 (2018).
33. C. Wang *et al*., In situ formed reactive oxygen species–responsive scaffold with gemcitabine and checkpoint inhibitor for combination therapy. *Sci. Transl. Med.* **10**, eaan3682 (2018).
34. J. Tang *et al*., Cardiac cell–integrated microneedle patch for treating myocardial infarction. *Sci. Adv.* **4**, eaat9365 (2018).
35. J. W. Lee, M. R. Prausnitz, *Drug Delivery Using Microneedle Patches: Not Just for Skin* (Taylor & Francis, 2018).